Satellite ice extent, sea surface temperature, and atmospheric methane trends in the Barents and Kara Seas

Ira Leifer[1], F. Robert Chen[2], Frank Muller Karger[2], Leonid Yurganov[3], Thomas McClimans[4]

[1] Bubbleology Research International, Inc., Solvang, CA, US. ira.leifer@bubbleology.com

[2] University of Southern Florida, US

[3] University of Maryland, Baltimore, US

[4] SINTEF Ocean, Trondheim, Norway

Supplementary Material

S1. Review of Airborne Arctic Methane measurements

CH_4 concentration profiles over the Arctic Ocean were measured on five flights during the HIAPER Pole-to-Pole Observations (HIPPO) campaign (Kort et al., 2012; Wofsy, 2011) and produced evidence of sea surface CH_4 emissions from the northern Chukchi and Beaufort Seas in most profiles, up to 82°N. Enhanced concentrations near the sea surface were common over fractured floating ice in sample profiles collected on 2 Nov. 2009, 21 Nov. 2009, and 15 Apr. 2010. On 13 Jan. 2009 and 26 Mar. 2010, when the seasonally highest level of sea-ice coverage occurred, CH_4 emissions were weak or non-existent. Some of the observational variability was correlated with carbon monoxide (CO), indicating terrestrial origin.

The Carbon in Arctic Reservoirs Vulnerability Experiment (CARVE) program sought to quantify Alaskan CO_2 and CH_4 fluxes between the atmosphere and surface terrestrial ecosystems. Intensive aircraft campaigns with ground-based observations were conducted during summer from 2012-2015 (Chang et al., 2014). No open ocean measurements were made. Additional Alaskan airborne data were collected summer 2015 (Jun.-Sept.) by the Atmospheric Radiation Measurements V on the North Slope of Alaska (ARM-ACME) project (38 flights, 140 science flight hours), with vertical profile spirals from 150 m to 3 km over Prudhoe Bay, Oliktok Point, Barrow, Atqasuk, Ivotuk, and Toolik Lake. Continuous data on CO_2, CH_4, CO, and nitrous oxide, N_2O, were collected (Biraud, 2016).

West of Svalbard, an area of known widespread seabed CH_4 seepage aligned along a north-south fault parallel to the coast (Mau et al., 2017; Westbrook et al., 2008) was the focus of a field airborne campaign June–July 2014 (Myhre et al., 2016). Flights were conducted using the Facility for Airborne Atmospheric Measurements (FAAM) of the Natural Environment Research Council (NERC, UK). The campaign measured a suite of atmospheric trace gases and was coordinated with oceanographic observations. Seabed CH_4 seepage led to significantly increased seawater CH_4 concentrations. However, no significant atmospheric CH_4 enhancement was observed for the region above the seeps for summer data collected 20 Jun.–1 Aug. 2014 (Myhre et al., 2016) under mostly light winds.

S2. Satellite Arctic AIRS and IASI Methane Measurement and Validation

A number of current orbital TIR instruments observe CH_4 (Jacob et al., 2016) including the Tropospheric Emission Spectrometer (TES) (Worden et al., 2012), the Cross-Track Infrared Sounder (CrIS) (Gambacorta, 2013), InfraRed Atmospheric Sounder Interferometer (IASI) (Clerbaux et al., 2009), and the Atmospheric Infrared Sounder (AIRS) (Aumann et al., 2003b).

IASI CH_4 validation has been addressed in a number of studies for the lower and mid-upper Arctic troposphere. The EuMetSat IASI instruments are cross-track-scanning Michelson interferometers onboard the MetOp-A and MetOp-B platforms (Clerbaux et al., 2009). IASI-1 (2007-) and IASI-2 (2013-) follow sun synchronous orbits. Three IASI New Generation instruments (Crevoisier et al., 2014) are planned for launch in 2021, 2028, and 2035 (IASI-NG, 2017).

IASI instruments measure in 8461 channels at 0.5 cm^{-1} spectral resolution from three spectrometers spanning 645 to 2760 cm^{-1}. These spectrometers have a 2×2 array of circular footprints with a nadir spatial resolution of 12 km that is 39×25 km at swath (2400 km) maximum (Clerbaux et al., 2009). IASI-1 was launched into an 817 km-altitude polar orbit on 19 Oct. 2006, while IASI-2 was launched on 17 Sept. 2012. MetOp-A and MetOp-B cross the equator at approximately 09:30 and 21:30 local time, separated by approximately half an orbit, resulting in twice daily, near-global coverage with 29-day revisit. The on-flight noise-equivalent delta temperature at 280K is estimated to be well below 0.1K in the spectral range of interest to CH_4 (Razavi et al., 2009). IASI has a wide swath with a scan angle of ±48.3°. IASI CH_4 retrieval algorithms are described by Xiong et al. (2013) and Gambacorta (2013).

In the TIR, the AIRS (Atmospheric InfraRed Sounder) mission onboard the Earth Observation Satellite, Aqua satellite (Aumann et al., 2003b) and the EuMetSat IASI-1 mission, on the MetOp-A platform (Crevoisier et al., 2014) (Clerbaux et al., 2009) provide long-term arctic CH_4 observations with new IASI instruments planned for launch in 2021, 2028, and 2035 (IASI-NG, 2017).

AIRS is a grating diffraction nadir cross-track scanning spectrometer on the Aqua satellite (2002-) that is part of the Earth Observation System (Aumann et al., 2003a). AIRS was launched into a 705-km-altitude polar orbit on the EOS Aqua spacecraft on 4 May 2002. The satellite crosses the equator at approximately 01:30 and 13:30 local time, producing near global coverage twice a day, with a scan angle of ±48.3°. Effective field of view after cloud clearing, is 45 km (Susskind et al., 2006) and the CH_4 spectral resolution is 1.5 cm^{-1} from the 7.8 μm TIR channel (Aumann et al., 2003b). Version 6 of AIRS Levels 2 and 3 data are publicly available (AIRS, 2016); see Xiong et al. (2010) for a description, evaluation, and validation of global CH_4 AIRS retrievals. Lower-troposphere (0-4 km altitude averaged) AIRS profiles are analyzed herein because the AIRS time series is longer than IASI.

AIRS CH_4 validation has been addressed in Xiong et al. (2010), who compared aircraft data taken over Poker Flat, Alaska, and Surgut, Siberia with AIRS CH_4 retrieved profiles. Agreement was within 1.2% with mean measured CH_4 concentration between 300–500 hPa; correlation coefficients were ~0.6-0.7.

IASI validation (Xiong et al., 2013) over a large area was achieved during a quasi pole-to-pole flight of the National Science Foundation's Gulfstream V aircraft (Wofsy, 2011). A bias of nearly -1.74% was found for 374–477 hPa and -0.69% for 596–753 hPa. Yurganov et al. (2016) compared 5-year long IASI data for 0-4 km layer over a sea area adjacent to the Zeppelin Observatory, Svalbard, Norway, at 474 m altitude, operated by the Norwegian Institute for Air Research (NILU). Monthly mean values and monthly trends were in good agreement, but daily excursions did not correlate. Yurganov et al. (2016) explained the latter by the observatory's location being near the top of the planetary boundary layer.

S3. Detailed Currents and Bathymetry

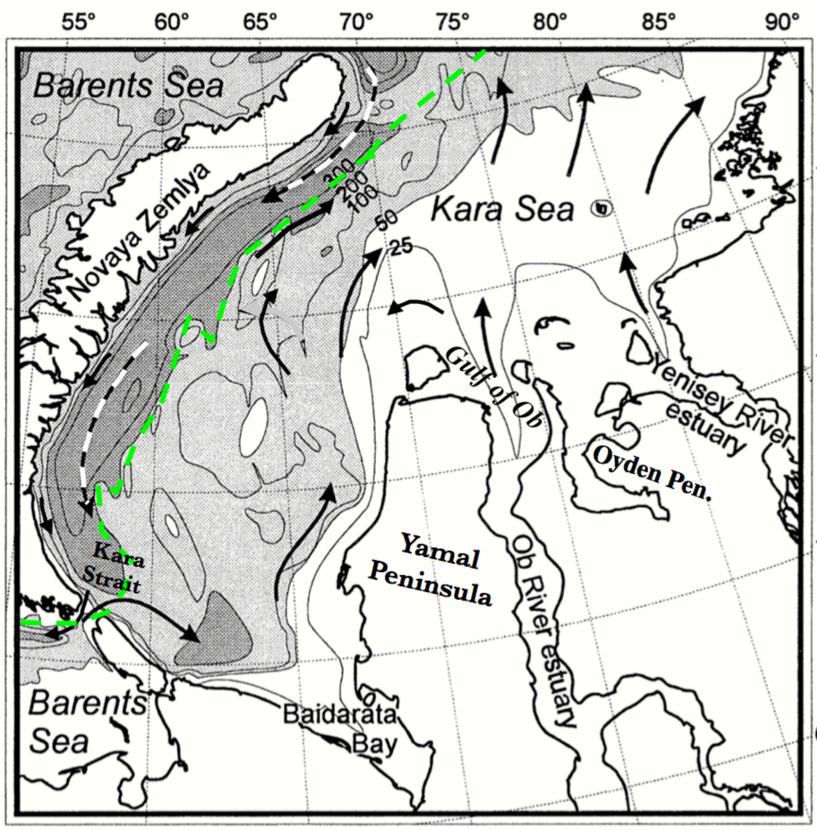

Figure S1. Bathymetry and currents for the Kara Sea. Adapted from Polyak et al. (2002) and McClimans et al. (2000). Dashed line indicates subsurface flows. Green line shows approximate edge of submerged permafrost from Osterkamp (2010).

In the Kara Sea, the outflows of the Ob and Yenisei Rivers (350 and 650 km^3 yr^{-1}, respectively (Stedmon et al., 2011), are very important causing it to be mostly brackish and extremely shallow due to sediment deposition. Combined with inflow from the Barents Sea, currents for most of the Kara Sea are largely northwards. The exception is the more than 300 m deep Novaya Zemlya Trough where water enters from the north Barents Sea and flows below the brackish surface waters.

Cold Arctic waters, and ice and melt water from Novaya Zemlya flow southward along the eastern shore of the Novaya Zemlya Archipelago in the narrow, weak Novaya Zemlya Coastal Current (NZCC). Inflow of modified

Atlantic water from the Barents Sea (dashed line in Fig. S1) accounts for a warm core in the deep Novaya Zemlya Trough (see McClimans et al., 2000, Section 11). Part of the NZCC exits through the same Kara Strait that Barents Sea coastal water enters. This, in combination with the rising shallow seabed, causes the Kara Strait to be a site of strong mixing.

The Ob and Yenisei Rivers transport significant sediment, underlying the shallowness of the Kara Sea, with extensive proven and proposed petroleum hydrocarbon reservoirs underlying the east and southeast Kara Sea (Rekacewicz, 2005). Given the Kara Sea's shallowness, CH_4 seep seabed bubbles can mostly transfer their gas directly to the atmosphere (Leifer et al., 2017; Leifer and Patro, 2002) and indirectly from wind mixing (Wanninkhof and McGillis, 1999), and also from storm sparging (Boitsov et al., 2012; Shakhova et al., 2013), which in the Arctic can extend to 100-200 m depth, i.e., most of the Kara Sea.

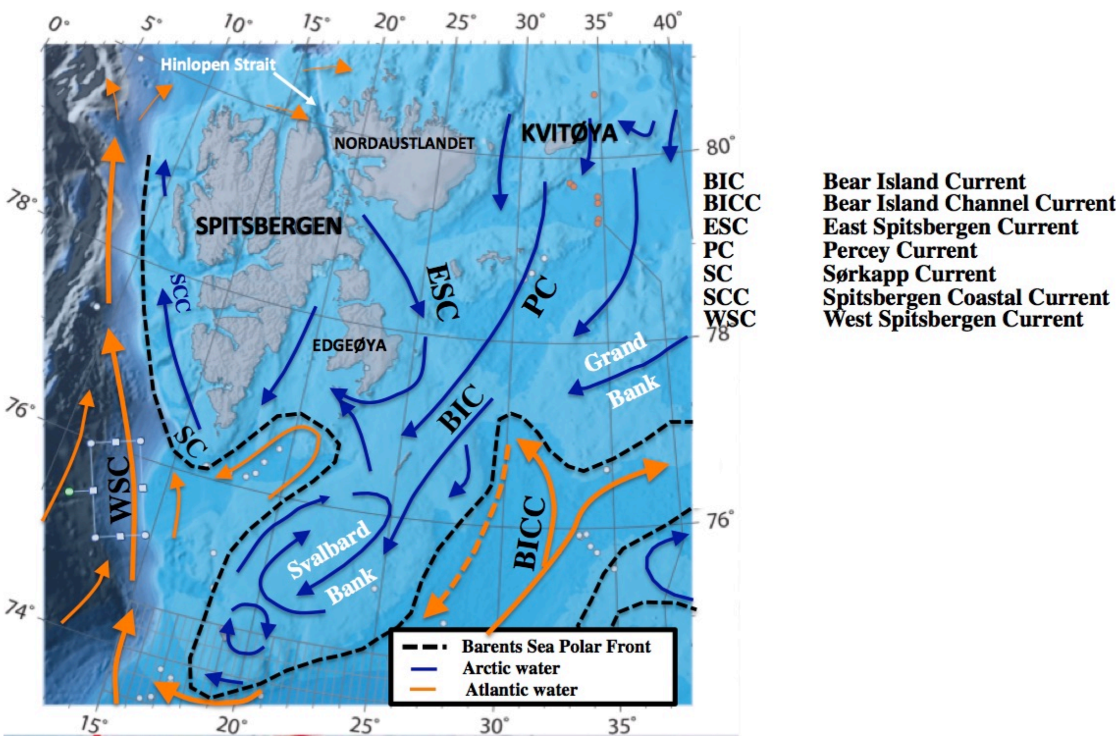

Figure S2. Bathymetry and currents around Svalbard. Bathymetry from Norwegian Petroleum Directorate (2016). Currents from Loeng (1991). Dashed black line shows location of the Barents Sea Polar Front, Dashed currents are submerged; blue - cold, orange - warm.

Currents and flows around Svalbard Archipelago are complex (**Fig. S2**), dominated by the West Spitsbergen Current (WSC), which is the northerly fork of the Norwegian Atlantic Current (NAC), and flows northwards off the west coast of Spitsbergen. The cold, Percey Current (PC) flows southwest off the eastern shores of the Svalbard Archipelago. The cold East Spitsbergen Current (ESC) flows through the Hinlopen Strait and then joins the PC to flow around the south cape of Spitsbergen as the Sørkapp Current (SC), following the coast northwards as the Spitsbergen Coastal Current (SCC) (Svendsen et al., 2002). The cold SCC flows inshore of the WSC, and flows up Svalbard's western coast, inshore and shallower than the warm, Atlantic WSC. The interface between these two currents off west Spitsbergen forms a part of the Barents Sea Polar Front. Thus, coastal waters offshore West Spitsbergen are of Barents Sea / Atlantic water origin, whereas further offshore lies Barents Sea water (origin Atlantic Ocean).

The location of the Barents Sea Polar Front (Oziel et al., 2016) is semi-permanent and controlled by seabed topography (**Fig. S2**), particularly the Svalbard Bank, the Great Bank, and the trough south of Spitsbergen.

S4. Winds and Currents in the Barents and Kara Sea

The energy budget of the Barents Sea is driven by Atlantic heat input by the two forks of the NAC (**Fig. S3**) (Lien et al., 2013), strongly impacting the Barents Sea *SST* climatology (**Fig. S3**). Along one fork, warmer water flows eastward along the northern Norwegian, Murman, and then western Novaya Zemlya coasts towards the north. The other NAC fork flows northeast along the Svalbard Bank (SB). These flows closely correspond to "tendrils" of warmer water extending north to the east of the Central Bank and to the west of Novaya Zemlya and around Bear Island (**Fig. S3a**) and in September in the east Barents Sea (**Fig. S3b**). In June, winds oppose this climatology, i.e., *SST* is most strongly influenced by ocean current transport. In fall, currents and winds are aligned along the Norwegian and Murman and western Novaya Zemlya coasts, reinforcing the transport of heat as indicated in *SST*. Note, though much of the heat that these winds transport originates from the NAC, which maintains Norway at temperatures well above latitudinal averaged. Still, winds cannot explain the spatial distribution of warm *SST*, which extends into the calm around the Central Bank.

Water becomes cooler as it penetrates eastward, and as it reaches the (seasonally varying) ice edge (**Fig. S3**). Across much of the Barents Sea there is a strong latitudinal *SST* gradient extending south from the ice edge, independent of the location of the eastern NAC branches. In the coastal waters off western Novaya Zemlya, where the warm NZC flows, water extends further north than elsewhere into areas where winds are from the north (**Fig. 4a**). Moreover, regions with statistically significant warming *SST* trends (*dSST*/*dt*) were in areas of northerly winds both in June and September.

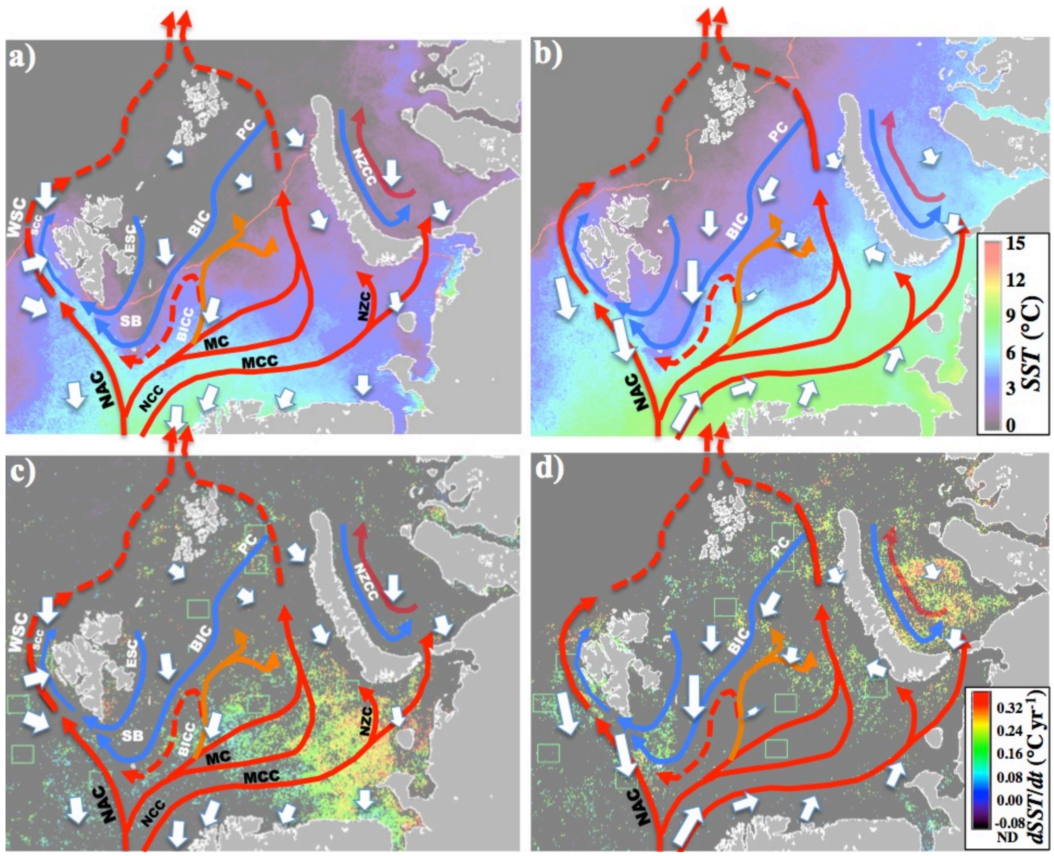

Figure S3. Warm and cold currents (from **Fig. 4a**) superimposed on **a)** June and **b)** September for climatology *SST*, and **c)** June and **d)** September for *dSST*/*dt* trends (ND-no trend detected). The red line shows ice location. Red and blue arrows show warm and cold currents, respectively. Dashed line indicates subsurface flow. Winds (white arrows) are adapted from Kolstad (2008).

Accessible meteorological data for the Barents Sea, outside of west Svalbard, whose meteorology and oceanography are affected by the Greenland Sea, are difficult to find, e.g., Boitsov et al. (2012) for Bear Island, except for sites on the northern Norwegian and Murman coasts. In this regard, the Murmansk airport weather data are the most eastward available long-term data representing southern Barents Sea, coastal meteorology and oceanography. Daily average meteorology data for 2002-2018 were downloaded (https://www.wunderground.com/weather/ru/murmansk) and segregated by month, and found a warming of 0.12°C yr^{-1} in June and 0.11°C yr^{-1} in September. Over this period, winds strengthened slightly (0.0173 m s^{-1} yr^{-1}) with most of the increase in September occurring in 2017 and 2018 (**Fig. S4**). These warming rates are significantly faster than those at Bear Island, which reflects both the greater moderation of the marine rather than coastal atmosphere and the influence of the cold Bear Island Current. Winter temperatures increased even faster.

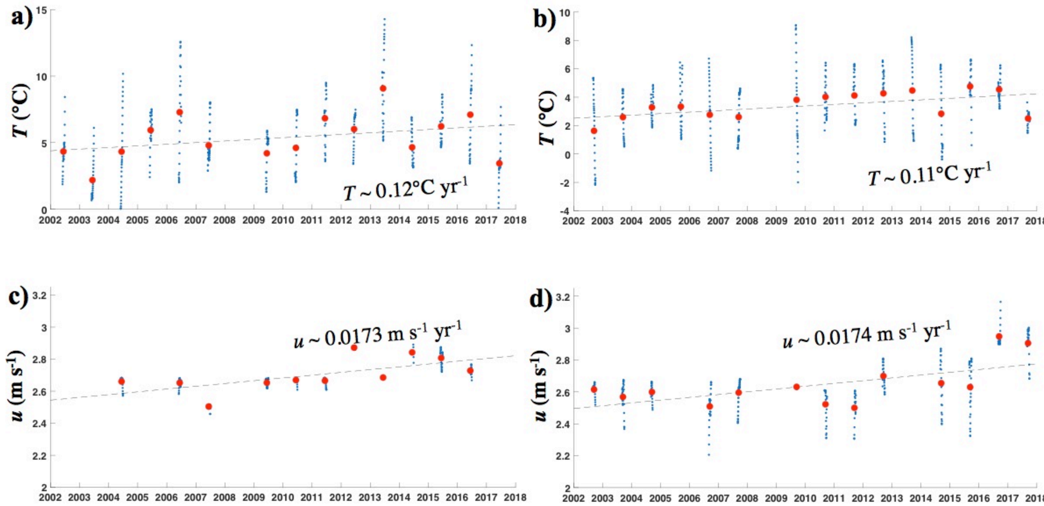

Figure S4. Wind and temperatures for Murmansk airport, Murman, Russia (68.7845°N, 32.7579°E) for **a)** June and **b)** September. Daily-averaged (blue) and monthly-averaged (red) data, and linear polynomial fits (red dashed line) are shown. Data from weatherunderground.com.

S5. Barents Sea *in situ* data

CO_2 and CH_4 *in situ* data were collected by a Cavity Enhanced Absorption Spectrometer (CEAS), Greenhouse Gas Analyzer (Los Gatos, Research, Mountainview, CA) onboard the *R/V Akademik Fyodorov* during the Nansen and Amundsen Basins Observational System (NABOS) expedition in fall 2013. The *R/V Akademik Fyodorov* is 141-m long with a 25-m beam and 8-m draught. The *R/V Akademik Fyodorov* departed Kirkenes, Norway on 21 Aug. 2013, returning to Kirkenes on 23 Sept. 2013. Analyzer performance information also was recorded for data quality review. Instrument precision was ~1 ppb with a 10 s response time and a 117 s mean layback time. Samples were collected from above the main superstructure, approximately 25 m above the sea surface (**Fig. S4a**), Calibration was daily and used a cylinder standard provided by the Norwegian Air Research Institute (NILU).

The main potential source of ship pollution could be the diesel engine exhaust; however, it appears that the *Akademik Fyodorov*'s engine is not a source of CH_4, with atmospheric CH_4 partially oxidized by the engine leading to exhaust gas having depressed CH_4 compared to ambient air. Data analyzed herein were during steaming transit across the Barents Sea at 26 km hr^{-1}, for which other potential vessel sources, such as the sewage storage venting are not relevant.

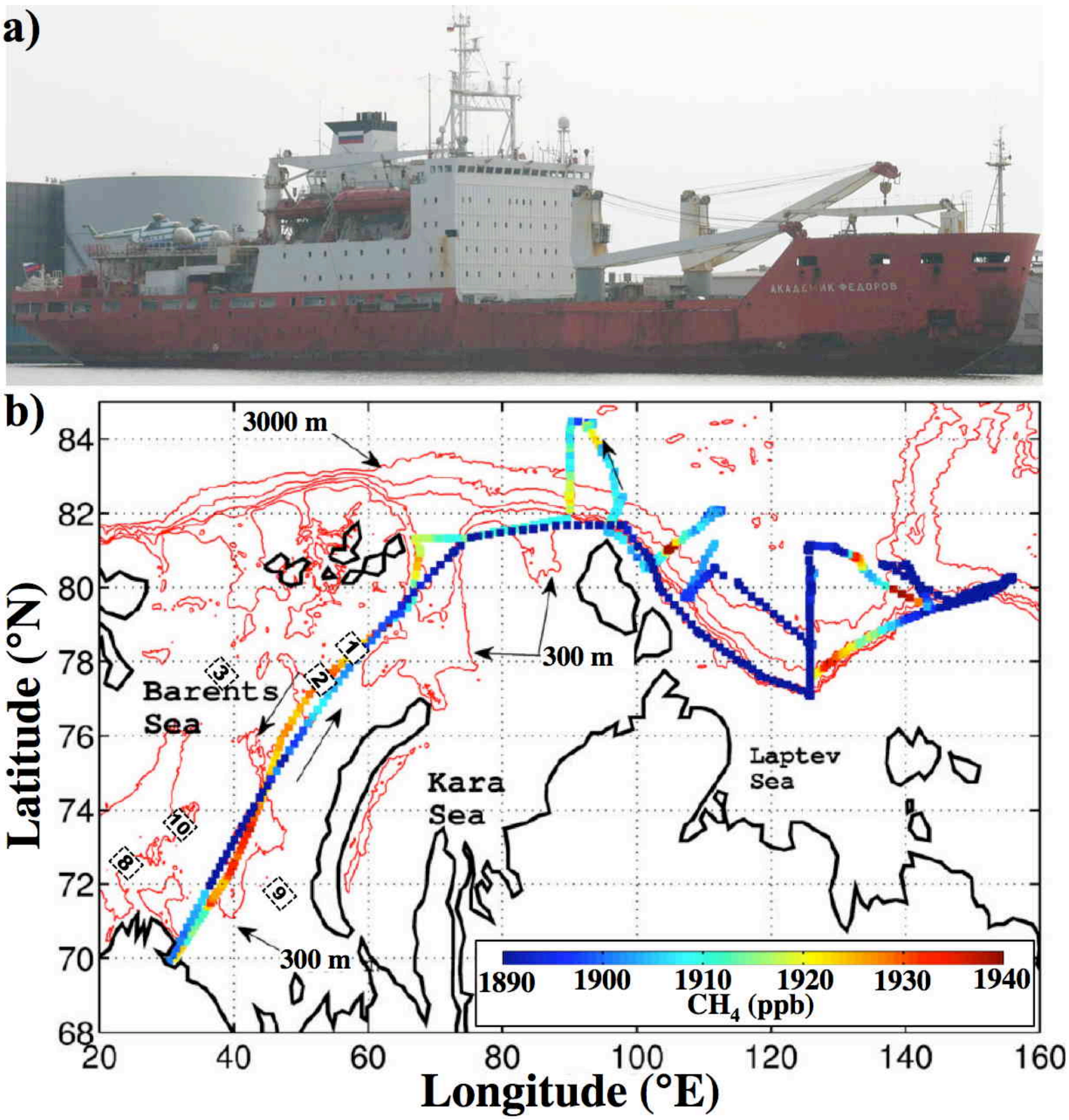

Figure S5. a) Photo of the *R/V Akademic Fyodorov*. **b)** Hourly averaged methane (CH_4) from NABOS expedition. Red shows 300 m depth of the hydrate stability field. Location of focus areas (**Table S1**) shown. Data key on figure.

The month-long data set showed a significant difference between the northwards and southwards transits of the Barents Sea, which were separated by approximately one month and passed directly through Focus areas 1 and 2, as well as between focus areas 9 and 10 in the southeast Barents Sea, approximately along the path of the Murman Current. Most of the CH_4 values in the Laptev Sea were low, although there were several locations of enhanced CH_4.

NABOS values were compared with satellite-retrieved column CH_4 from IASI for 21-24 Aug. 2013 for the northeastwards transit and for 17-22 Sept. 2013 for the southwestwards transit. Agreement between IASI lower tropospheric CH_4 and *in situ* CH_4 for the northwards transit was good, within ~10 ppb, whereas agreement was much poorer for the southwards transit.

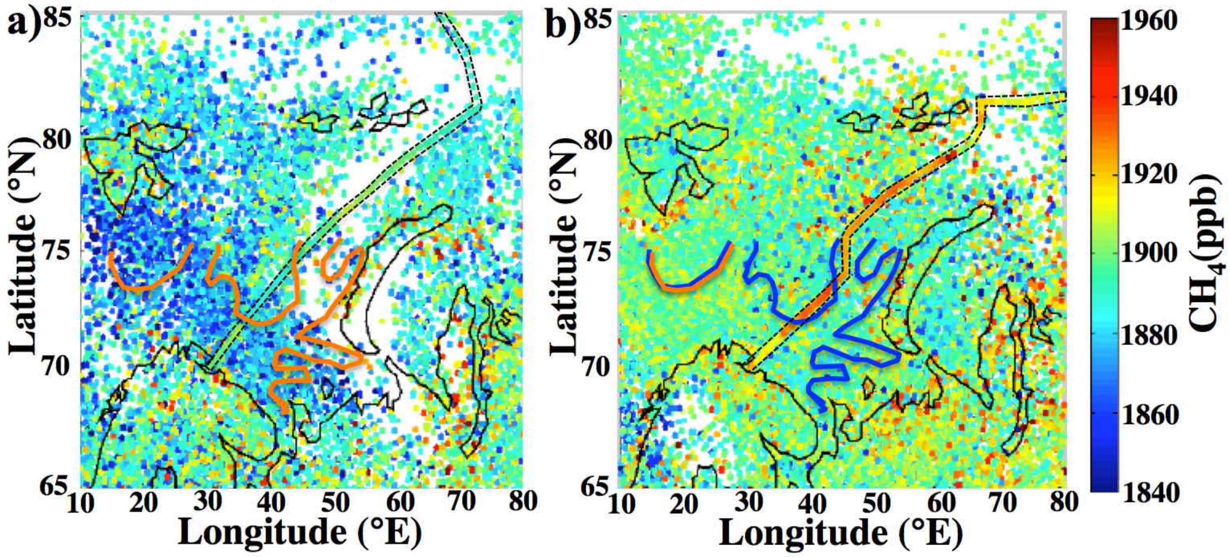

Figure S6. a) IASI retrieved 0-4 km methane (CH_4) for 21-24 Aug. 2013 and hourly CH_4 from the NABOS cruise (outlined in dashed line black). Also shown is the Murman Coastal Current's edges in orange and blue from Alexeev et al. (2018) and **b)** for 17-22 Sept. 2013. Data key on figure.

S6. Focus Areas

Table S1. Focused study area coordinates

Area	Upper Left	Upper Right	Lower Left	Lower Right
1	79° 16'6.91" N 60° 48'53.42" E	78° 32'12.26" N 62° 49'54.69" E	78° 55' 5.27" N 57° 43' 42.58" E	78° 12'27.81" N 59° 52'32.46" E
2	78° 38'25.09" N 55° 34'48.90" E	77° 56'45.71" N 57° 48'15.36" E	78° 14' 20.21" N 52° 49' 55.73" E	77° 34'0.24" N 55° 8'13.34" E
3	79° 10'4.24" N 41° 13'50.40" E	78° 36'13.19" N 44° 21'38.03" E	78° 38' 35.38" N 38° 57' 26.67" E	78° 6'12.61" N 42° 3'28.98" E
4	79°38'46.04" N 5° 40'51.21" E	79° 31'53.40" N 10° 11'25.49" E	78° 57' 49.65" N 5° 19' 46.85" E	78° 51'21.95" N 9° 34'7.45" E
5	78° 8'40.32" N 0° 36'30.89" E	78° 6'24.41" N 4° 35'53.20" E	77° 27' 29.19" N 0° 34' 31.46" E	77° 25'20.57" N 4° 20'54.29" E
6	76° 11'22.21" N 1° 16'10.96" E	76° 8'46.20" N 4° 41'44.27" E	75° 30' 6.27" N 1° 12'35.25" E	75° 27'37.48" N 4° 28'29.63" E
7	74° 48'24.40" N 12° 40'7.63" E	74° 36'9.07" N 15° 40'42.21" E	74° 8' 1.53" N 12° 7'35.64" E	73° 56'16.20" N 15° 1'6.10" E
8	73° 34'52.37" N 33° 48'43.77" E	73° 6'7.85" N 36° 8'55.31" E	73° 0'12.51" N 32° 31'37.62" E	72° 32'23.29" N 34° 49'20.56" E
9	72° 46'29.04" N 48° 59'20.20" E	72° 8'6.72" N 50° 44'6.03" E	72° 18'49.49" N 47° 18'49.40" E	71° 41'23.16" N 49° 4'27.27" E
10	74° 48'6.77" N 38° 38'57.13" Ë	74° 16'3.18" N 41° 0'24.96" E	74° 15'28.49" N 37° 5'34.21" E	73° 44'27.53" N 39° 25'24.39" E

S7. Summer month sea surface temperature and methane trends

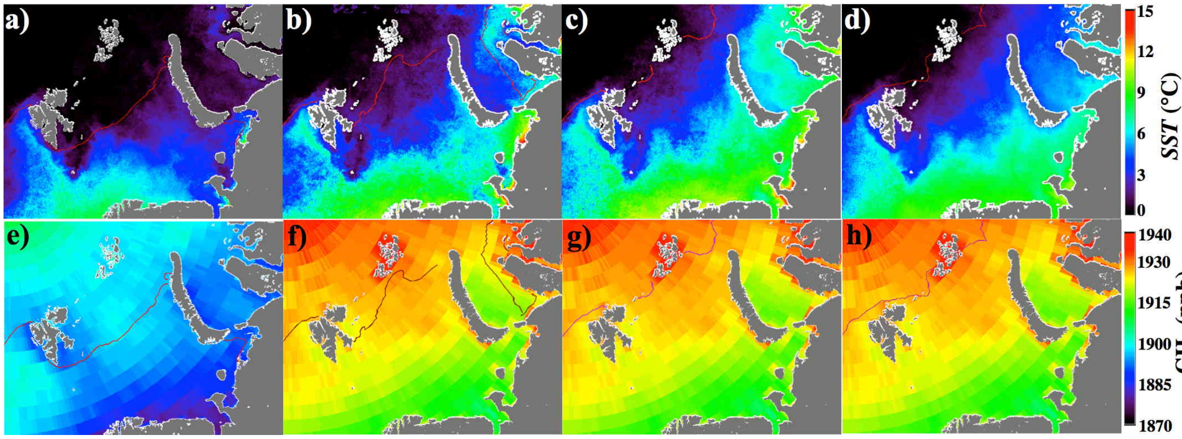

Figure S7. Mean values for 2003 to 2015 of sea surface temperature (*SST*) for **a**) June, **b**) July, **c**) August, and **d**) September. Mean methane (CH_4) concentration for **e**) June, **f**) July, **g**) August, and **h**) September. Median ice edge for same period is shown. Years with reduced ice extent contribute to values of *SST* north of the ice edge. Data keys on figure.

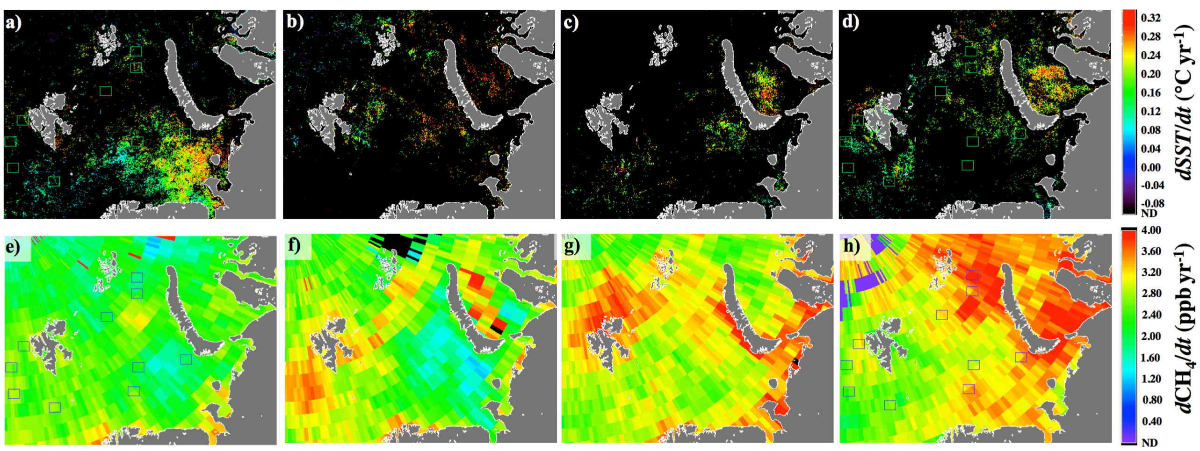

Figure S8. Linear trends for 2003 to 2015 of sea surface temperature ($dSST/dt$) for **a**) June, **b**) July, **c**) August, and **d**) September. Methane concentration trend (dCH_4/dt) for **e**) June, **f**) July, **g**) August, and **h**) September. ND – not detectable, i.e., failed statistical test. Blue, black dashed lines shows 100 and 50 m contour, respectively. Data key on figure.

S8. Barents and Kara Seas Oil and Gas Reservoirs

The Barents and Kara seas contain significant and extensive oil and gas reserves, which in the case of the Russian Kanin Peninsula extend onshore where they are produced and transported by pipeline (**Fig. S9**). Additional extensive proven hydrocarbon resources are found in the shallow southwest Kara Sea (Rise et al., 2015). It is likely, given the relationship between major river outflows and hydrocarbon reserves globally (e.g., the Mississippi, the Amazon, the Congo, the Nile) that similar reserves underlie the shallow northeastern Kara Sea.

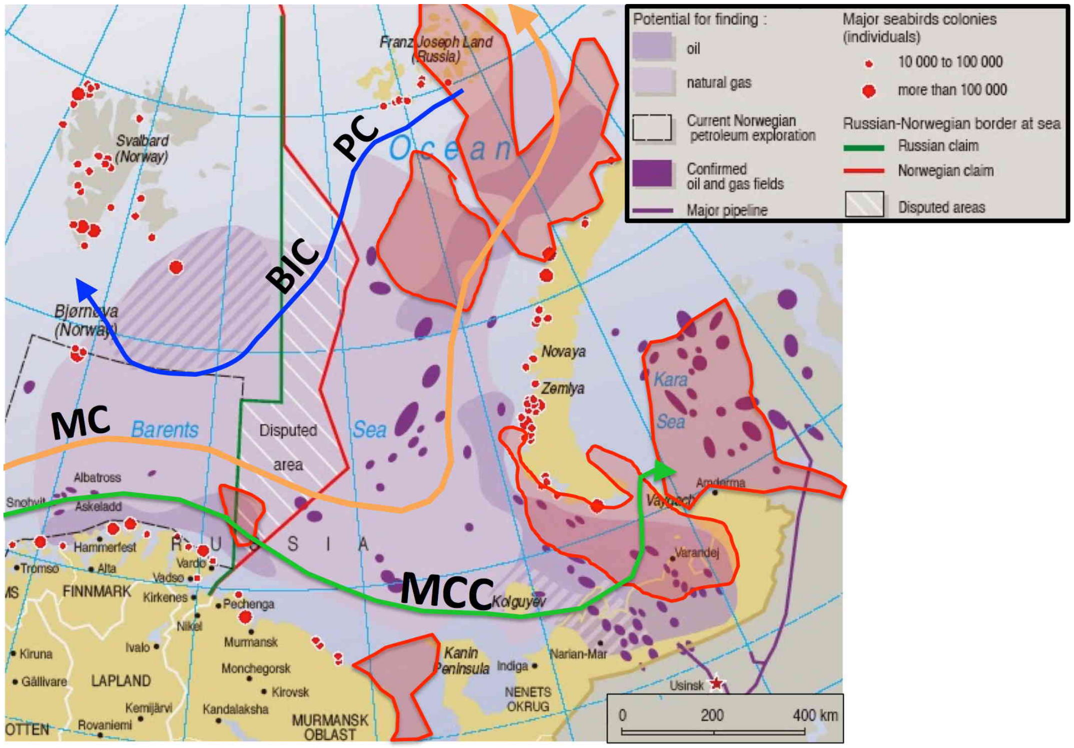

Figure S9. Barents Sea location of oil and gas fields and potential fields, and pipelines. Also shown are the approximate locations of the major Barents Sea currents – the Murman Current (MC), Murman Coastal Current (MCC), Bear Island Current (BIC), and Percey Current (PC). Outlined in red are areas where dCH_4/dt > 3 ppb yr^{-1} from **Fig. 11**. Adapted from Rekacewicz (2005).

S9. Arctic Methane Movie

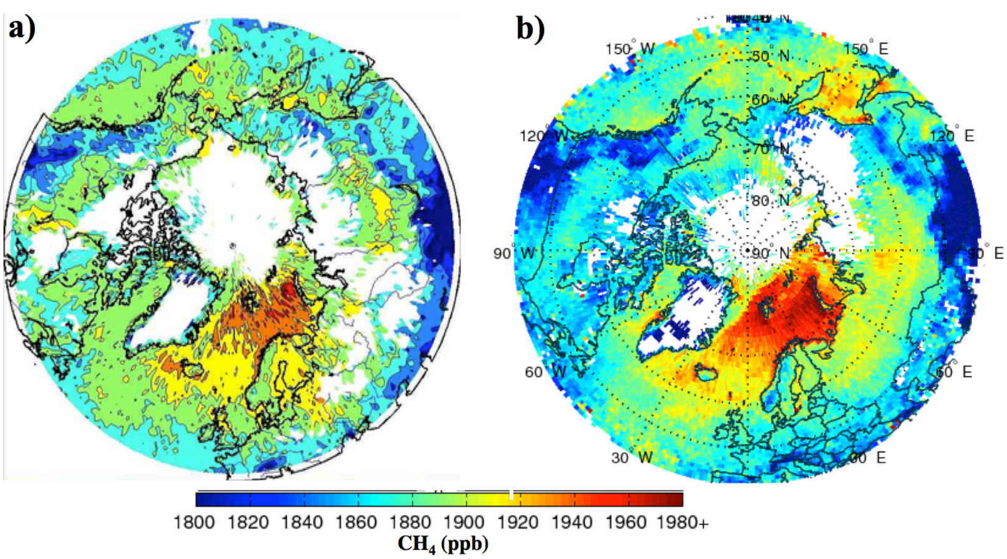

Figure S10. IASI Arctic methane (CH_4) for the lower 4 km for a) March 2012 and b) March 2018.

A movie of Arctic CH_4 from 2012 every 5 days shows a range of variations on a range of different spatial and temporal scales. Strong enhancements are observed that persist in regions for a few days–most likely related to synoptic system flushing in fall to spring. The seasonal variation is easily observed, with highest values often in November and December. In late winter and early spring, large CH_4 anomalies are observed in some years at the ice edge.

Supplemental References

AIRS: http://airs.jpl.nasa.gov/data/v6/, http://airs.jpl.nasa.gov/data/v6/, 2016.

Alexeev, A. P., et al.: http://www.pinro.ru/labs/hid/kolsec1_e.htm, last access: 25 March 2018 2018.

Aumann, H. H., et al.: AIRS/AMSU/HSB on the Aqua mission: design, science objectives, data products, and processing systems, IEEE Transactions on Geoscience and Remote Sensing, 41, 253-264, 2003a, doi: 10.1109/TGRS.2002.808356.

Aumann, H. H., et al.: AIRS/AMSU/HSB on the Aqua mission: design, science objectives, data products, and processing systems, IEEE Transactions on Geoscience and Remote Sensing, 41, 253-264, 2003b, doi: 10.1109/TGRS.2002.808356.

Biraud, S. C.: ARM-ACME V: ARM Airborne Carbon Measurements V on the North Slope of Alaska Field Campaign Report, DOE Office of Science Atmospheric Radiation Measurement (ARM) Program (United States), 15 pp., 2016.

Boitsov, V. D., Karsakov, A. L., and Trofimov, A. G.: Atlantic water temperature and climate in the Barents Sea, 2000–2009, ICES Journal of Marine Science, 69, 833-840, 2012, doi: 10.1093/icesjms/fss075.

Chang, R. Y.-W., et al.: Methane emissions from Alaska in 2012 from CARVE airborne observations, Proceedings of the National Academy of Sciences, 111, 16694-16699, 2014, doi: 10.1073/pnas.1412953111.

Clerbaux, C., et al.: Monitoring of atmospheric composition using the thermal infrared IASI/MetOp sounder, Atmospheric Chemistry and Physics, 9, 6041-6054, 2009, doi: 10.5194/acp-9-6041-2009.

Crevoisier, C., et al.: Towards IASI-New Generation (IASI-NG): Impact of improved spectral resolution and radiometric noise on the retrieval of thermodynamic, chemistry and climate variables, Atmospheric Measurement Techniques, 7, 4367-4385, 2014, doi: 10.5194/amt-7-4367-2014.

Gambacorta, A.: The NOAA Unique CrIS/ATMS Processing System (NUCAPS): Algorithm Theoretical Basis Documentation, NOAA, NOAA Center for Weather and Climate Predication, 78 pp., 2013.

IASI-NG: https://iasi-ng.cnes.fr/en/IASI-NG/index.htm, last access: 1 June 2017 2017.

Jacob, D. J., et al.: Satellite observations of atmospheric methane and their value for quantifying methane emissions, Atmospheric Chemistry Physics Discussion, 16, 14371-14396, 2016, doi: 10.5194/acp-16-14371-201.

Kolstad, E. W.: A QuikSCAT climatology of ocean surface winds in the Nordic seas: Identification of features and comparison with the NCEP/NCAR reanalysis, Journal of Geophysical Research: Atmospheres, 113, D11106, 2008, doi: 10.1029/2007JD008918.

Kort, E. A., Frankenberg, C., Miller, C. E., and Oda, T.: Space-based observations of megacity carbon dioxide, Geophysical Research Letters, 39, L17806, 2012, doi: 10.1029/2012GL052738.

Leifer, I., Chernykh, D., Shakhova, N., and Semiletov, I.: Sonar gas flux estimation by bubble insonification: Application to methane bubble flux from seep areas in the outer Laptev Sea, The Cryosphere, 11, 1333-1350, 2017, doi: 10.5194/tc-11-1333-2017.

Leifer, I. and Patro, R.: The bubble mechanism for methane transport from the shallow seabed to the surface: A review and sensitivity study, Continental Shelf Research, 22, 2409-2428, 2002, doi: 10.1016/S0278-4343(02)00065-1.

Lien, V. S., Vikebø, F. B., and Skagseth, Ø.: One mechanism contributing to co-variability of the Atlantic inflow branches to the Arctic, Nature Communications, 4, 1488, 2013, doi: 10.1038/ncomms2505.

Loeng, H.: Features of the physical oceanographic conditions of the Barents Sea, Polar Research, 10, 5-18, 1991, doi: 10.1111/j.1751-8369.1991.tb00630.x.

Mau, S., et al.: Widespread methane seepage along the continental margin off Svalbard - from Bjørnøya to Kongsfjorden, Scientific Reports, 7, 42997, 2017, doi: 10.1038/srep42997.

McClimans, T. A., et al.: Transport processes in the Kara Sea, Journal of Geophysical Research: Oceans, 105, 14121-14139, 2000, doi: 10.1029/1999JC000012.

Myhre, C. L., et al.: Extensive release of methane from Arctic seabed west of Svalbard during summer 2014 does not influence the atmosphere, Geophysical Research Letters, 43, 2016GL068999, 2016, doi: 10.1002/2016GL068999.

Norwegian Petroleum Directorate: Resource Report, Norwegian Petroleum Directorate,, Stavanger, Norway, 56 pp., 2016.

Osterkamp, T. E.: Subsea Permafrost. In: Climate and Oceans, Steele, J. H., Thorpe, S. A., and Turekian, K. K. (Eds.), Academic Press, London UK, 2010.

Oziel, L., Sirven, J., and Gascard, J. C.: The Barents Sea frontal zones and water masses variability (1980–2011), Ocean Science, 12, 169-184, 2016, doi: 10.5194/os-12-169-2016.

Polyak, L., et al.: Benthic foraminiferal assemblages from the Southern Kara Sea - A river-influenced Arctic marine environment, The Journal of Foraminiferal Research, 32, 252-273, 2002, doi: 10.2113/32.3.252.

Razavi, A., et al.: Characterization of methane retrievals from the IASI space-borne sounder, Atmospheric Chemistry and Physics, 9, 7889-7899, 2009, doi: 10.5194/acp-9-7889-2009.

Rekacewicz, P.: https://www.grida.no/resources/7482) last access: January 2018 2018.

Rise, L., Bellec, V. K., Chand, S., and Bøe, R.: Pockmarks in the southwestern Barents Sea and Finnmark fjords, Norwegian Journal of Geology, 94, 263-282, 2015, doi: 10.17850/njg94-4-02.

Shakhova, N., et al.: Ebullition and storm-induced methane release from the East Siberian Arctic Shelf, Nature Geoscience, 7, 64-70, 2013, doi: 10.1038/ngeo2007.

Stedmon, C. A., Amon, R. M. W., Rinehart, A. J., and Walker, S.: The supply and characteristics of Colored Dissolved Organic Matter (CDOM) in the Arctic Ocean: Pan Arctic trends and differences, Marine Chemistry, 124, 108-118, 2011, doi: 10.1016/j.marchem.2010.12.007.

Susskind, J., et al.: Accuracy of geophysical parameters derived from Atmospheric Infrared Sounder/Advanced Microwave Sounding Unit as a function of fractional cloud cover, Journal of Geophysical Research: Atmospheres, 111, D09S17, 2006, doi: 10.1029/2005JD006272.

Svendsen, H., et al.: The physical environment of Kongsfjorden–Krossfjorden, an Arctic fjord system in Svalbard, Polar Research, 21, 133-166, 2002, doi: 10.1111/j.1751-8369.2002.tb00072.x.

Wanninkhof, R. and McGillis, W. R.: A cubic relationship between air-sea CO_2 exchange and wind speed, Geophysical Research Letters, 26, 1889-1892, 1999, doi, http://www.scopus.com/inward/record.url?eid=2-s2.0-0032735098&partnerID=40.

Westbrook, G. K., et al.: Estimation of gas hydrate concentration from multi-component seismic data at sites on the continental margins of NW Svalbard and the Storegga region of Norway, Marine and Petroleum Geology, 25, 744-758, 2008, doi: 10.1016/j.marpetgeo.2008.02.003.

Wofsy, S. C.: HIAPER Pole-to-Pole Observations (HIPPO): fine-grained, global-scale measurements of climatically important atmospheric gases and aerosols, Philosophical Transactions of the Royal Society A: Mathematical, Physical and Engineering Sciences, 369, 2073-2086, 2011, doi: 10.1098/rsta.2010.0313.

Worden, J., et al.: Profiles of CH4, HDO, H2O, and N2O with improved lower tropospheric vertical resolution from Aura TES radiances, Atmospheric Measurement Techniques, 5, 397-411, 2012, doi: 10.5194/amt-5-397-2012.

Xiong, X., et al.: Mid-upper tropospheric methane retrieval from IASI and its validation, Atmospheric Measurement Techniques, 6, 2255-2265, 2013, doi: 10.5194/amt-6-2255-2013.

Xiong, X., et al.: Mid-upper tropospheric methane in the high Northern Hemisphere: Spaceborne observations by AIRS, aircraft measurements, and model simulations, Journal of Geophysical Research: Atmospheres, 115, D19309, 2010, doi: 10.1029/2009jd013796.

Yurganov, L., Leifer, I., and Lund-Myhre, C.: Seasonal and interannual variability of atmospheric methane over Arctic Ocean from satellite data, Current Problems in Remote Sensing of Earth from Space (Sovremennye Problemy Distantsionnogo Zondirovaniya Zemli iz Kosmosa), 13, 107-119, 2016, doi: 10.21046/2070-7401-2016-13-2-107-119.